Wiley Analytical Science

The Current State of Reconstruction Technologies for 3D X-ray Microscopy including Algorithmic Innovation for AI-based Recovery

April 26, 10:00am - 11:00am EDT

Many properties can only be fully understood in 3D, such as porosity and tortuosity in porous materials, network connection maps in neuroscience, or mechanical properties in 3D additively manufactured structures. X-ray microscopy provides a unique method to image samples non-destructively in 3D across a wide range of materials and life sciences.

Watch this session during the WAS Virtual Conference:

Nicolas Guenichault, Ph.D.

Dr. Stephen T. Kelly, Ph.D.

Register Now

This talk is sponsored by **ZEISS**

Dispersion-Enabled Symmetry Switching of Photonic Angular-Momentum Coupling

Jixiang Cai, Fei Zhang, Mingbo Pu,* Yan Chen, Yinghui Guo, Ting Xie, Xingdong Feng, Baoshan Jiang, Xiaoliang Ma, Xiong Li, Honglin Yu, and Xiangang Luo*

Photonic spin-orbit interactions describe the interactions between spin angular momentum and orbital angular momentum of photons, which play essential roles in subwavelength optics. However, the influence of frequency dispersion on photonic angular-momentum coupling is rarely studied. Here, by elaborately designing the contribution of the geometric phase and waveguide propagation phase, the dispersion-enabled symmetry switching of photonic angular-momentum coupling is experimentally demonstrated. This notion may induce many exotic phenomena and be found in enormous applications, such as the spin-Hall effect, optical calculation, and wavelength division multiplexing systems. As a proof-of-concept demonstration, two metadevices, a multi-channel vectorial vortex beam generator and a phase-only hologram, are applied to experimentally display optical double convolution, which may offer additional degrees of freedom to accelerate computing and a miniaturization configuration for optical convolution without collimation operation. These results may provide a new opportunity for complex vector optical field manipulation and calculation, optical information coding, light-matter interaction manipulation, and optical communication.

1. Introduction

Light carries both linear and angular momenta at the macroscopic and single-photon scales. Therefore, the interaction between light and matter inevitably involves a momentum exchange.[1,2] Specifically, the linear momentum of a photon can be expressed as $\hbar/\lambda$ (λ is the wavelength), and the angular momentum includes two different components, i.e., spin angular momentum (SAM) and orbital angular momentum

(OAM).[2,3] The SAM possesses two values, $\pm\hbar$ per photon, associated with the handedness of the circular polarization, while OAM has unlimited values of $l\hbar$ (l is the topological charge) per photon, depending on the spatial profile of light intensity and phase.[4] To describe the interplay and mutual conversion between SAM and OAM, the optical spin-orbit interactions (SOIs) were first proposed in 1992 by Liberman and Zel'dovich.[5,6] Since the cycleaveraged linear momentum density (**p**) and angular momentum density (**j**) can be described by $\mathbf{j} = \mathbf{r} \times \mathbf{p}$ ($\times$ and **r** indicate cross product and radius vector, respectively),[7] it is possible to manipulate SOIs through changing the wavelength of incident light.

Metasurfaces, as the 2D equivalent of metamaterials, can flexibly manipulate the properties of electromagnetic waves through the collective contributions of subwavelength particle arrays with different orientations, dimensions, and materials.[8–10] It is worth noting that metasurfaces can provide a natural platform for enhancing SOIs, including symmetric and asymmetric SOIs.[11,12] For symmetric SOIs, commonly showing spin symmetry, could produce the geometric phase (GP) of $\pm\zeta\alpha$ (ζ is related to lattice and rotational symmetries of meta-atoms, and α is the orientation angle) through the coupling of the SAM and coordinate frame rotation.[13,14] The symmetric SOIs have yielded various applications, such as broadband spin-Hall

J. Cai, F. Zhang, M. Pu, Y. Chen, Y. Guo, T. Xie, X. Feng, X. Li, X. Luo
State Key Laboratory of Optical Technologies on Nano-Fabrication and Micro-Engineering
Institute of Optics and Electronics
Chinese Academy of Sciences
Chengdu 610209, China
E-mail: pmb@ioe.ac.cn; lxg@ioe.ac.cn
J. Cai, H. Yu
Key Laboratory of Opto-electronic Technology and Systems of the Education Ministry of China
Chongqing University
Chongqing 400044, China

F. Zhang, M. Pu, Y. Chen, Y. Guo
Research Center on Vector Optical Fields
Institute of Optics and Electronics
Chinese Academy of Sciences
Chengdu 610209, China
M. Pu, Y. Guo, X. Ma, X. Li, X. Luo
School of Optoelectronics University of Chinese Academy of Sciences
Beijing 100049, China
B. Jiang
Tianfu Xinglong Lake Laboratory
Chengdu 610299, China

effect,[15] ultrafast optical pulse shaping,[16] among many others.[17–19] Especially, catenary-shaped continuous structures developed from catenary optics can broaden the bandwidth and angular range of SOIs,[17] resulting in many high-performance functional devices like flat wide-angle imaging with ~180° diffraction-limited field of view.[17,20] Recently, asymmetric SOIs have shown excellent capabilities in the independent manipulation of left-handed and right-handed circularly polarized (LCP and RCP) light by combining the GP and the waveguide propagation phase (WPP). This provides an unprecedented opportunity for vector optical field manipulation,[21,22] asymmetric transmission,[11,23] photonic angular momentum generation and detection,[24,25] and holography.[26,27] The switching of photonic angular-momentum coupling has attracted significant attention due to its compactness, flexibility, and versatility, which has been implemented by phase-change material for optical information storage and encryption.[24] Nevertheless, the influence of frequency dispersion on photonic angular-momentum coupling suffers through insufficient investigation in research.

In this work, the concept of dispersion-enabled symmetry switching of photonic angular-momentum coupling is proposed. To verify this concept, the spin- and wavelength-dependent double convolution is experimentally demonstrated with metasurfaces. Such a double convolution method can exactly superimpose the vortex beams between different channels by controlling the spin states and wavelengths of the incident light, and could promote the miniaturization of the optical system without additional devices and overcome difficulties in collimation. Moreover, another meta-hologram device is designed and fabricated to further verify the double convolution scheme. We believe that this approach possesses great potential for wave processors, wavelength division multiplexing systems, and vector optical field manipulation and calculation.

2. Concept and Metasurface Design

Figure 1 is the conceptual illustration of the dispersion-enabled symmetry switching of photonic angular-momentum coupling for multi-channel OAM beams. The symmetric and asymmetric SOIs are switched by the wavelengths of the incident light, which causes different electromagnetic responses for diverse spin states of light. For symmetric SOIs, three-channel OAM beams with l_m ($l_1 = -2$, $l_2 = 1$, $l_3 = 0$) and corresponding phase distribution of $\Phi_{\lambda 1}$ are obtained for RCP incidence at 10.6 μm wavelength, while its centrosymmetric image with $-l_m$ emerges for LCP incidence. Benefiting from asymmetric SOIs, another different three-channel OAM beams with l_n ($l_4 = 0$, $l_5 = 0$, $l_6 = 1$) and phase distribution of $\Phi_{\lambda 2}$ can be observed under LCP incidence at 9.3 μm wavelength. Eventually, nine-channel OAM beams are produced for RCP illumination based on a convolution process $\mathcal{F}[\exp(i\Phi_{\lambda 1})] \otimes \mathcal{F}[\exp(i\Phi_{\lambda 1})] \otimes \mathcal{F}[\exp(i\Phi_{\lambda 2})]$, where $\mathcal{F}$ denotes the Fourier transform and $\otimes$ indicates the convolution operator. Note that this process (named double convolution) includes two steps, the first and second convolution, in which corresponding convolution kernels are $\mathcal{F}[\exp(i\Phi_{\lambda 1})]$ and $\mathcal{F}[\exp(i\Phi_{\lambda 2})]$, respectively. Practically, it can be regarded as the exact superpositions of topological charge and intensity of each OAM beam of convolution kernels, which is controlled by its wave vector k along the x- and y-direction. Besides, the channel number of OAM beams will expand from 3 to 9, and the information is encoded in these channels.

In conventional optical systems, the implementation of optical convolution commonly relies on the 4f-system or two orthogonal gratings based on the Talbot effect.[28–30] However, the substantial limitations of cumbersome volume and difficulties in collimation for two lenses/gratings hinder its further applications in integrated optical or photo-electric systems. These restrictions likewise exist in the metasurface-based
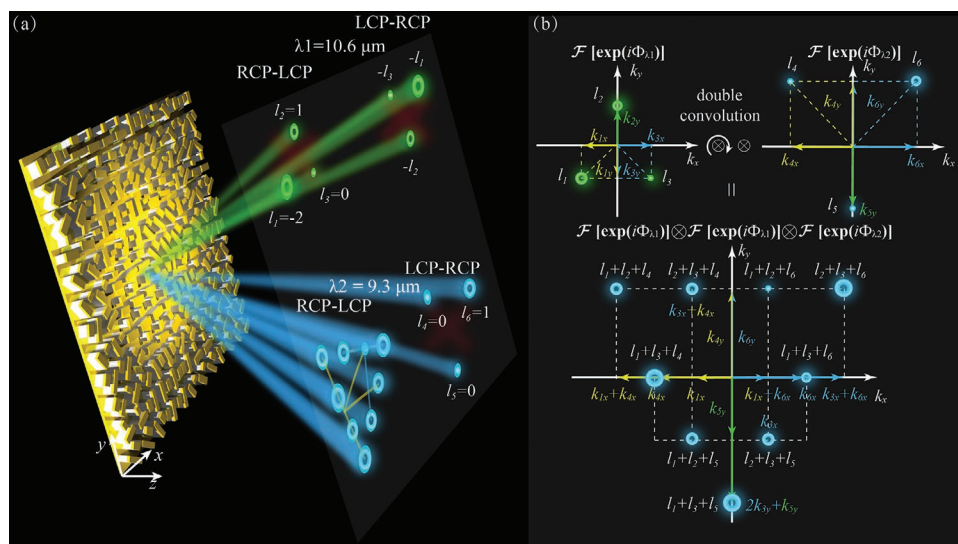
Figure 1. Schematic illustration of the dispersion-enabled symmetry switching of photonic angular-momentum coupling for double convolution with a multi-channel OAM generator. a) Optical performances of the multi-channel OAM generator illuminated by LCP and RCP light at the wavelength of 9.3 μm (bottom) and 10.6 μm (top), respectively. b) Process of double convolution for the two phase distributions ($\Phi_{\lambda 1}$ and $\Phi_{\lambda 2}$), in which $\mathcal{F}[\exp(i\Phi_{\lambda 1})]$ and $\mathcal{F}[\exp(i\Phi_{\lambda 2})]$ are the convolution kernels for the first and second convolution, respectively. The LCP-RCP represents that the incident LCP light is converted to the reflected RCP light, and the RCP-LCP has a similar definition.

optical convolution systems.[31–35] Moreover, the spin- and wavelength-dependent convolution is hard to be implemented due to the constraints, such as principle restrictions and intrinsic characteristics. Therefore, this double convolution process may provide extra degrees of freedom to accelerate computing and further stimulate the development and utilization of parallelized wave processors and wavelength division multiplexing systems.[36,37]

To reveal the physical mechanism in Figure 1, it is necessary to analyze the optical properties of a single anisotropic element. Each anisotropic metal-insulator-metal (MIM) element is considered as a local wave plate, which maximally converts incident circularly polarized (CP) light into reflected light with the opposite helicity. For simplicity, we assume a lossless anisotropic element that introduces phase shifts of $\beta\pm\delta/2$, representing the WPP along its major and minor axes, respectively. δ is the WPP difference between the two axes, and it affects the polarization conversion efficiency.[11] β represents the WPP difference among different elements. The Jones matrix of this element can be described as $\mathrm{diag}[\exp(i\beta+i\delta/2), \exp(i\beta-i\delta/2)]$. By performing a rotation of the element's orientation angle α with respect to the x-direction, the reflection Jones matrix $\mathbf{M}$ in the helicity basis has the explicit form:[39]

$$\mathbf{M} = \exp(i\beta)\begin{bmatrix} \cos\dfrac{\delta}{2} & i\sin\dfrac{\delta}{2}\exp(i2\alpha) \\ i\sin\dfrac{\delta}{2}\exp(-i2\alpha) & \cos\dfrac{\delta}{2} \end{bmatrix} \quad (1)$$

In this case, when the arbitrarily polarized beam $\boldsymbol{E}_i$ normally impinges on the metasurface from the $+z$-direction, the electric field of reflected beams $\boldsymbol{E}_r$ can be written as:

$$\mathrm{E}_r = \mathbf{M}\mathrm{E}_i = \cos\frac{\delta}{2}\exp(i\beta)\mathrm{E}_i - i\sin\frac{\delta}{2}\times$$
$$\left[\langle\mathrm{E}_i | R\rangle\exp(-i2\alpha+i\beta)| L\rangle + \langle\mathrm{E}_i | L\rangle\exp(i2\alpha+i\beta)| R\rangle\right] \quad (2)$$

where $|L\rangle = (0\ 1)^T$ and $|R\rangle = (1\ 0)^T$ represent LCP and RCP components, respectively. From the second term of Equation (2), the cross-polarized reflection component carries not only the spin-dependent and dispersion-free GP of $\pm2\alpha$, but also the spin-independent and dispersion-controlled WPP of β. Note that such an additional WPP can provide an opportunity for breaking the SOI symmetry and revealing dispersion-dependent features. Therefore, when the WPP only responds to one wavelength channel but vanishes at another wavelength, it is possible to realize dispersion-enabled symmetry switching of photonic angular-momentum coupling. Thus, the reflected optical fields $\mathbf{E}_{r1}$ and $\mathbf{E}_{r2}$ corresponding to symmetric and asymmetric SOIs for two different wavelengths can be expressed as:

$$\mathrm{E}_{r1} = \langle\mathrm{E}_i | R\rangle\exp(-i2\alpha)| L\rangle + \langle\mathrm{E}_i | L\rangle\exp(i2\alpha)| R\rangle \quad (3)$$

$$\mathrm{E}_{r2} = \langle\mathrm{E}_i | R\rangle\exp(-i2\alpha+i\beta)| L\rangle + \langle\mathrm{E}_i | L\rangle\exp(i2\alpha+i\beta)| R\rangle \quad (4)$$

Here, we set $\Phi_{\lambda1} = -2\alpha$ (only related to the GP). By adjusting the local orientation of elements, $\Phi_{\lambda1}$ can cover the full 2π range and eventually constitute symmetric SOIs. Furthermore,

by simultaneously changing the dimensions and orientations of various elements, asymmetric SOIs can be achieved through the collaboration of the GP and WPP, i.e., setting $\Phi_{\lambda2} = 2\alpha + \beta$.[18,25]

The optical Fourier transform is adopted to observe the patterns in momentum space.[40,41] Here, the Fourier transform of optical fields $\mathbf{E}_{r2}$ of the first term in Equation (4) can be written as:

$$\mathcal{F}[\exp(-i2\alpha+i\beta)] = \mathcal{F}[\exp(i2\Phi_{\lambda1}+i\Phi_{\lambda2})] \approx$$
$$\{\mathcal{F}[\exp(i\Phi_{\lambda1})]\otimes\mathcal{F}[\exp(i\Phi_{\lambda1})]\otimes\mathcal{F}[\exp(i\Phi_{\lambda2})]\} \quad (5)$$

Obviously, the specific convolution in Equation (5), named double convolution, involves the first convolution of $\mathcal{F}[\exp(i\Phi_{\lambda1})]$ and itself, and the second convolution with $\mathcal{F}[\exp(i\Phi_{\lambda2})]$, in which the convolution kernels of double convolution are $\mathcal{F}[\exp(i\Phi_{\lambda1})]$ and $\mathcal{F}[\exp(i\Phi_{\lambda2})]$, respectively. Theoretical investigations elucidate that this configuration can achieve spin- and wavelength-dependent convolution, assuming that we generate arbitrary phase distributions of $\Phi_{\lambda1}$ and $\Phi_{\lambda2}$ at two different wavelengths.

To satisfy the abovementioned phase design conditions and maintain high cross-polarization conversion efficiency, we employ six MIM antennas presented in Table S1 (Supporting Information) to construct plasmonic reflection-type metasurfaces. The schematic illustration of one element is depicted in **Figure 2**a. Simulation results of the optimized six elements at 9.3 and 10.6 μm wavelengths are shown in Figure 2b,c. The cross-polarized amplitudes in Figure 2b exceed ~0.81 and ~0.85 on average at 9.3 and 10.6 μm wavelengths, respectively. As illustrated in Figure 2c, through dispersion control enabled by abundant structural parameters and catenary optical fields between two nanofins,[41] the WPP of the designed six elements can cover the full 2π range with $\pi/3$ phase interval at 9.3 μm wavelength. Meanwhile, it is almost unchanged at 10.6 μm wavelength. Therefore, the symmetric and asymmetric SOIs can be switched at two different wavelengths.[38] Furthermore, the GP is always twice the orientation angle of each element, which can be used to selectively decode predesigned coded information with the assistance of a polarization filter.
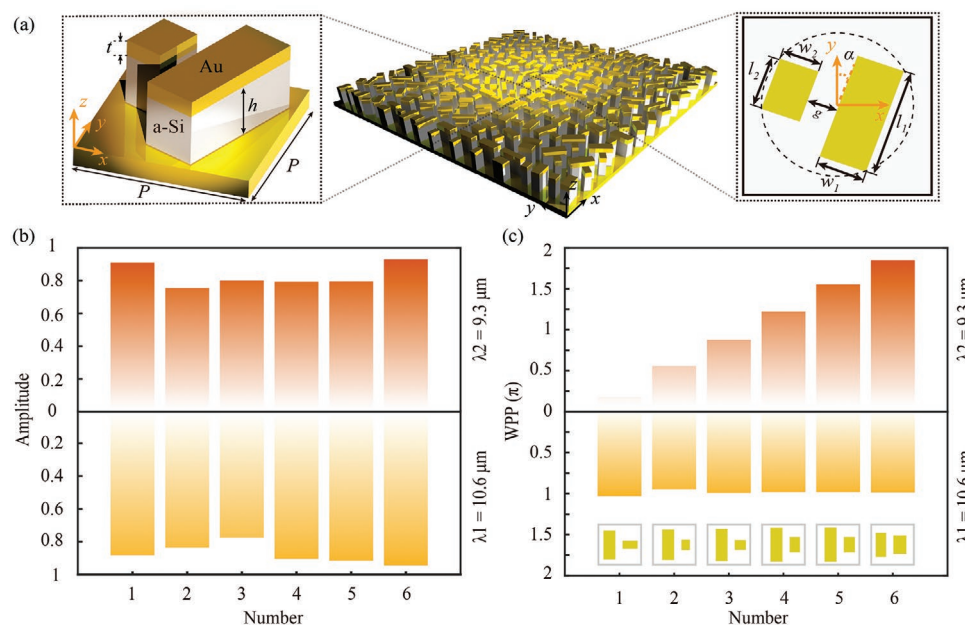
3. Characterization of Metadevices

To verify the double convolution in momentum space presented in Figure 1, the ultrathin multi-channel vortex generator is designed. Its complex electric field can be considered as the linear superimposition of the individual complex field of the OAM beam with different phase shifts, whose phase distributions can be described as follows:[42]

$$\Phi_{\lambda1;\lambda2}(x,\gamma) =$$
$$arg\left\{\sum_{m;n}a_{(m;n)}(x,\gamma)\exp\left\{-i[k_{(m;n)x}x+k_{(m;n)y}\gamma-l_{(m;n)}\varphi(x,\gamma)]\right\}\right\} \quad (6)$$

where m and n can be recognized as theoretically arbitrary integers for $\Phi_{\lambda1}$ and $\Phi_{\lambda2}$ to obtain multi-channel OAM beams, respectively. Here, we set $m = 1, 2, 3$ and $n = 4, 5, 6$. $a_{(m;n)}(x,\gamma)$ represents the amplitude component of individual OAM

ADVANCED
SCIENCE NEWS

www.advancedsciencenews.com

ADVANCED
FUNCTIONAL
MATERIALS

www.afm-journal.de

Figure 2. Design of the elements. a) Schematic illustration of the MIM element and its geometrical parameters are $t = 0.2$ μm, $h = 1.1$ μm, $P = 5$ μm. Simulation results of amplitudes b) and phase shifts c) of the selected six elements.
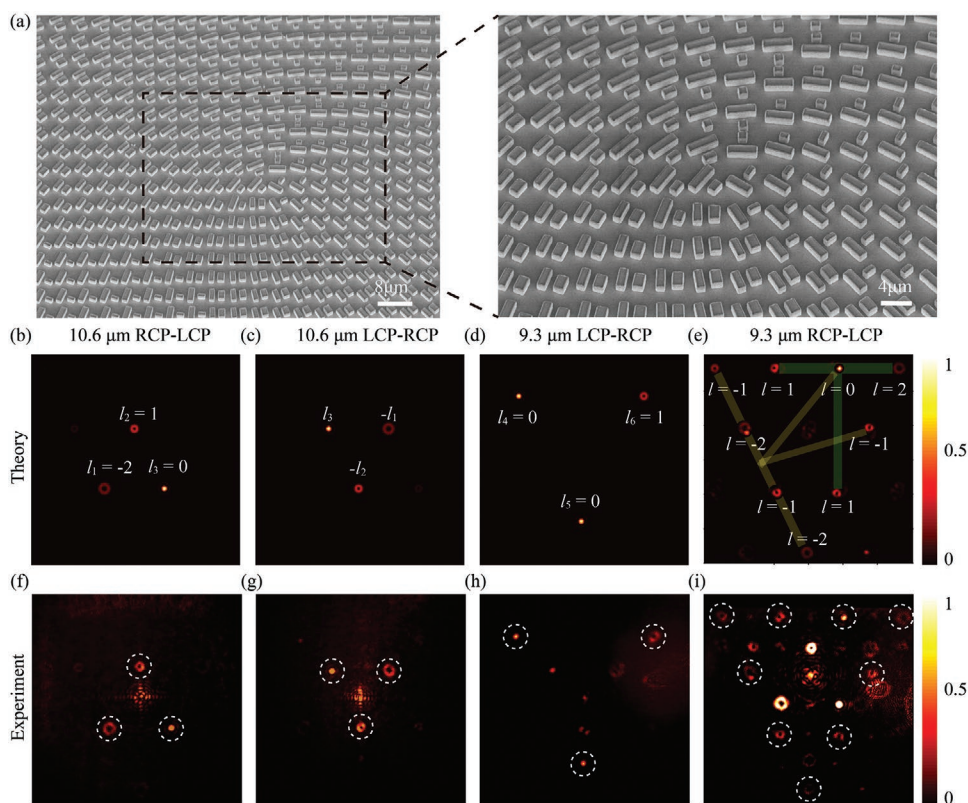
light, which determines its light intensity in the output plane. $k_{(m;n)x} = k\sin(\theta_{(m;n)x})$ and $k_{(m;n)y} = k\sin(\theta_{(m;n)y})$ are components of wave vector ($k = 2\pi/\lambda$, λ is equal to $\lambda1$ and $\lambda2$, respectively) along the x- and y-directions, respectively, in which $\theta_{(m;n)x}$ and $\theta_{(m;n)y}$ indicate the diffraction angles. $\varphi(x, y) = \tan^{-1}(y/x)$ means azimuth angle. The additional random phase is utilized to decrease the mutual interference between adjacent channels.

A metadevice for generating the multi-channel vectorial vortex beam is designed based on the relations of Φ-α, and the corresponding scanning electron microscopy (SEM) images are sketched in **Figure 3**a. Figure 3b–e presents the theoretical intensity profiles in momentum space under RCP and LCP illumination at the two different wavelengths. The intensity profiles of three-channel OAM beams with different topological charges of l_m ($l_1 = -2$, $l_2 = 1$, $l_3 = 0$) corresponding to the phase distribution of $\Phi_{\lambda1}$ are generated under the RCP incidence at 10.6 μm wavelength as shown in Figure 3b. Due to the symmetric SOIs, one centrosymmetric pattern with topological charges of $-l_m$ for LCP incidence is observed, as shown in Figure 3c. For asymmetric SOIs at 9.3 μm wavelength, another three-channel OAM beams with topological charges of l_n ($l_4 = 0$, $l_5 = 0$, $l_6 = 1$) and phase distribution $\Phi_{\lambda2}$ are obtained for LCP illumination in Figure 3d. The final information is encoded in the nine-channel OAM vector optical beam based on double convolution, in which such complex OAM vector optical beams with positive and negative topological charges compose "T" and tilt "K" in Figure 3e, respectively.

In fact, the double convolution process can be considered as the topological charge and intensity superposition controlled by wave vector (Figure S1, Supporting Information), i.e., complex vector optical field manipulation and calculation. Thus, optical convolution can be realized via predesigning the wave vector along the x- and/or y-direction of each OAM beam. In addition, all the topological charges can be directly identified

through dislocated interference fringes (Figure S2, Supporting Information), which demonstrates the correctness of topological charges superposition by double convolution. Note that the interference fringes with the same axial scales (from −2 to +2 mm) are generated by the interference of a titled plane wave and each OAM beam, respectively, in which these patterns seem in different axial scales due to the influence of the included angle between two beams (see Section S2, Supporting Information, for more details).[44] The measured intensity profiles in momentum space are illustrated in Figure 3f–i, which reveals good agreement with theoretical results in Figure 3b–e. The slight difference between simulation and measurement results can be observed in Figure 3h,i, which originates from the cross-polarized interference at 10.6 μm wavelength caused by the imperfection of fabrication and measurement errors. Such crosstalk may be suppressed by designing more elements instead of six elements in Figure 2 and increasing the size of the metadevice. Evidently, symmetric and asymmetric SOIs can be simultaneously implemented with one metasurface for the spin- and wavelength-dependent convolution. In principle, it can be employed to realize the optical convolution between arbitrary two multi-channel OAM beams after obtaining their phase distributions.

It is worth noting that the proposed scenario could also be utilized for phase-only holography. To demonstrate its versatility and high performance, a phase-only metahologram device is fabricated, and its SEM images are depicted in **Figure 4**a. As two arbitrary and independent information channels, phase profiles $\Phi_{\lambda1}$ and $\Phi_{\lambda2}$ corresponding to diamond-like (in Figure 4b) and three points (in Figure 4d) holographic images are obtained by the Gerchberg–Saxton algorithm, respectively. Similar to conventional holograms based on symmetric SOIs that utilize circular polarization multiplexing to generate two central symmetric images in transmission or reflection

**ADVANCED
SCIENCE NEWS**

www.advancedsciencenews.com

**ADVANCED
FUNCTIONAL
MATERIALS**

www.afm-journal.de

Figure 3. Demonstrations of multi-channel OAM beams double convolution. a) SEM images of the fabricated multi-channel OAM generator. The theoretical b–e) and measured f–i) intensity profiles under LCP and RCP incidence at the wavelengths of 9.3 and 10.6 μm. The constant background noise produced by thermal radiation has been removed.

fields,[45] two diamond-like patterns are observed under the illumination of LCP and RCP at the wavelength of 10.6 μm as displayed in Figure 4b,c. Affected by asymmetric SOIs at 9.3 μm wavelength, different diffraction patterns for LCP and RCP illumination are generated as shown in Figure 4d,e. Three bright dots in Figure 4d can be recognized as a convolution kernel for double convolution that exactly fixes the center locations of each convolution image. As a result, an image including three diamonds is encoded in Figure 4e by the proposed double convolution method.
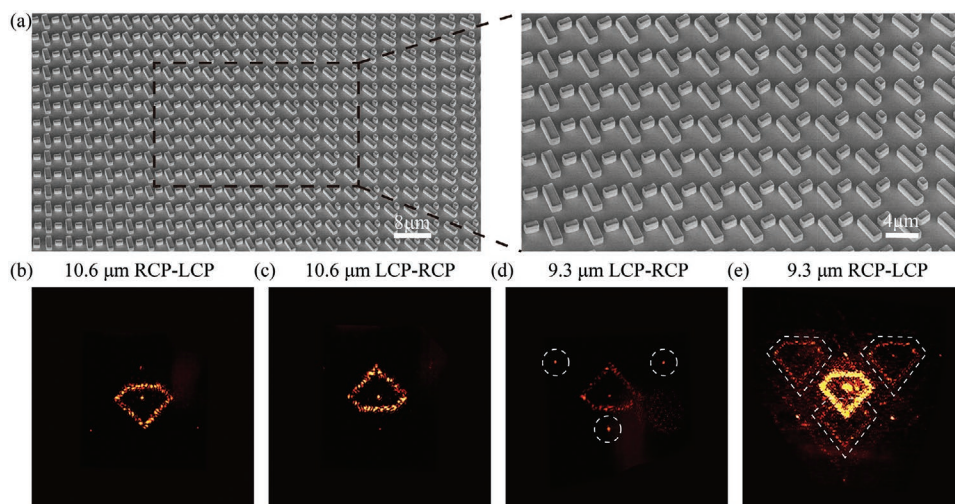
Figure 4. Demonstrations of double convolution holography. a) SEM images of the metahologram sample. b–e) Measured diffraction patterns generated by the designed metahologram under LCP and RCP illumination at the wavelengths of 9.3 and 10.6 μm. The constant background noise produced by thermal radiation has been removed.

**ADVANCED
SCIENCE NEWS**

www.advancedsciencenews.com

**ADVANCED
FUNCTIONAL
MATERIALS**

www.afm-journal.de

Furthermore, a holographic metadevice based on the point source algorithm is also experimentally demonstrated (Figure S3, Supporting Information). Different from the Gerchberg–Saxton algorithm, the point source algorithm can generate two non-centrosymmetric patterns under LCP and RCP incidence, even if the pure GP is adopted at the wavelength of 10.6 µm. The key is to synthesize a focused pattern and a conjugate divergent pattern (see Supporting Information, Section S3, for more details). Moreover, in order to quantify efficiency, a deflector is designed to diffract the incident LCP/RCP light to the +1st/−1st (+1st/+3rd) order with the diffraction efficiency of ~75%/~75% (~53.6%/63.7%) at 10.6 (9.3) µm wavelength, showing the high performance of double convolution as presented in Figure S4 (Supporting Information).

4. Conclusion

In summary, we present the concept of dispersion-enabled symmetry switching of photonic angular-momentum coupling. The phenomenon of double convolution, realizing spin- and wavelength-dependent optical convolution, is found between symmetric and asymmetric photonic spin-orbit interactions. Two double convolution metadevices are designed, fabricated, and demonstrated experimentally, which validate that different holographic images can be switched by changing the spin states and wavelengths of the incident light. It has been verified that such a scheme can transfer a simple light field into a complex vector light field via the vectorial optical calculation of periodic coherent superposition, resulting in the enhancement of information complexity and security. We believe that it may find extensive applications in wavelength division multiplexing systems, vector optical field manipulation and calculation, information coding, and so forth.

5. Experimental Section

Simulation: Numerical simulations were employed by the finite element method (FEM) in a commercial software package CST Microwave Studio to calculate cross-polarized reflectance and phase. The unit-cell boundary conditions were used along the *x*- and *y*-directions. For the *z*-direction, the open boundary conditions were employed. The material parameters of Au and a-Si were obtained from Palik's Handbook.[46]

Fabrication: The schematic diagram of the fabrication process is illustrated in Figure S5 (Supporting Information). First, a 5 nm thick Chromium (Cr) layer, a 300 nm thick gold (Au), a 1.1 µm thick amorphous Silicon(a-Si), and a 200 nm thick Au were sequentially deposited on the clean silicon (Si) wafer through magnetron sputtering. Then, a 500 nm thick positive photoresist (Pr) AZ1500 was spin-coated (2200 rpm) onto the film and baked at 100 °C for 10 min. Next, the elements were patterned by direct writing lithography to create an appropriate photoresist mask, and then it was transferred to the top Au layer by the ion beam etching (IBE). Finally, inductively coupled plasma (ICP) etching was utilized to etch the a-Si layer and remove the extra Pr. The metadevices for double convolution holography were generated, and their morphologic analysis was described by SEM.

Measurement: Figure S6 (Supporting Information) displays the schematic diagram of the measurement setup. The CO_2 laser was utilized as the light source. After passing through an adjustable attenuator, the optical beam was successively sent through a beam expander, a linear polarizer, and a quarter waveplate, followed by an adjustable aperture, and then illuminated on the sample from the top of the metadevices. In addition, the beam splitter was used in front of samples to guide the diffraction patterns to the infrared detector (CUBE817, Guide-Infrared Inc., 800×600 pixels), whose pixel size is 17 µm × 17 µm. The Fourier lens was inserted into the setup to realize Fourier transform for measuring holographic images in momentum space.

Conflict of Interest

The authors declare no conflict of interest.

Data Availability Statement

The data that support the findings of this study are available from the corresponding author upon reasonable request.

[1] A. Mair, A. Vaziri, G. Weihs, A. Zeilinger, *Nature* **2001**, *412*, 313.

[2] E. Hasman, *Nat. Nanotechnol.* **2010**, *5*, 563.

[3] C. Wu, S. Kumar, Y. Kan, D. Komisar, Z. Wang, I. B. Sergey, F. Ding, *Sci. Adv.* **2022**, *8*, eabk3075.

[4] P.-G. Chen, Z. Li, Y. Qi, T. W. Lo, S. Wang, W. Jin, K.-Y. Wong, S. Fan, A. V. Zayats, D. Lei, *ACS Nano* **2021**, *15*, 18171.

[5] V. S. Liberman, B. Y. Zel'dovich, *Phys. Rev. A* **1992**, *46*, 5199.

[6] P. Chen, T. W. Lo, Y. Fan, S. Wang, H. Huang, D. Lei, *Adv. Opt. Mater.* **2020**, *8*, 1901233.

[7] A. T. O'Neil, I. MacVicar, L. Allen, M. J. Padgett, *Phys. Rev. Lett.* **2002**, *88*, 053601.

[8] A. Arbabi, Y. Horie, M. Bagheri, A. Faraon, *Nat. Nanotechnol.* **2015**, *10*, 937.

[9] X. G. Luo, *Sci. China. Phys. Mech.* **2015**, *58*, 594201.

[10] H. Gao, Y. Wang, X. Fan, B. Jiao, T. Li, C. Shang, C. Zeng, L. Deng, W. Xiong, J. Xia, M. Hong, *Sci. Adv.* **2020**, *6*, eaba8595.

[11] F. Zhang, M. Pu, X. Li, P. Gao, X. Ma, J. Luo, H. Yu, X. Luo, *Adv. Funct. Mater.* **2017**, *27*, 1704295.

**ADVANCED
SCIENCE NEWS**

www.advancedsciencenews.com

**ADVANCED
FUNCTIONAL
MATERIALS**

www.afm-journal.de

[12] Y. Meng, Z. Liu, Z. Xie, R. Wang, T. Qi, F. Hu, H. Kim, Q. Xiao, X. Fu, Q. Wu, S.-H. Bae, M. Gong, X. Yuan, *Photonics Res.* **2020**, *8*, 564.

[13] K. Y. Bliokh, F. J. Rodríguez-Fortuño, F. Nori, A. V. Zayats, *Nat. Photonics* **2015**, *9*, 796.

[14] X. Xie, M. Pu, J. Jin, M. Xu, Y. Guo, X. Li, P. Gao, X. Ma, X. Luo, *Phys. Rev. Lett.* **2021**, *126*, 183902.

[15] X. G. Luo, M. B. Pu, X. Li, X. L. Ma, *Light Sci. Appl.* **2017**, *6*, 16276.

[16] S. Divitt, W. Zhu, C. Zhang, H. J. Lezec, A. Agrawal, *Science* **2019**, *364*, 890.

[17] M. Pu, X. Li, X. Ma, Y. Wang, Z. Zhao, C. Wang, C. Hu, P. Gao, C. Huang, H. Ren, X. Li, F. Qin, J. Yang, M. Gu, M. Hong, X. Luo, *Sci. Adv.* **2015**, *1*, 1500396.

[18] S. Wang, P. C. Wu, V. C. Su, Y. C. Lai, C. Hung Chu, J. W. Chen, S. H. Lu, J. Chen, B. Xu, C. H. Kuan, T. Li, S. Zhu, D. P. Tsai, *Nat. Commun.* **2017**, *8*, 187.

[19] Y. Wang, Q. Fan, T. Xu, *Opto-Electron. Adv.* **2021**, *4*, 200008.

[20] F. Zhang, M. B. Pu, X. Li, X. Ma, Y. Guo, P. Gao, H. Yu, M. Gu, X. Luo, *Adv. Mater.* **2021**, *33*, 2008157.

[21] X. Luo, F. Zhang, M. Pu, M. Xu, *J. Phys. Condens. Matter* **2022**, *34*, 381501.

[22] C. He, Y. Shen, A. Forbes, *Light Sci. Appl.* **2022**, *11*, 205.

[23] F. Zhang, M. Pu, Y. Guo, X. Ma, X. Li, P. Gao, X. Luo, *Sci. China Phys. Mech.* **2022**, *65*, 254211.

[24] S. Wang, Z.-L. Deng, Y. Wang, Q. Zhou, X. Wang, Y. Cao, B.-O. Guan, S. Xiao, X. Li, *Light Sci. Appl.* **2021**, *10*, 1.

[25] F. Zhang, X. Xie, M. Pu, Y. Guo, X. Ma, X. Li, J. Luo, Q. He, H. Yu, X. Luo, *Adv. Mater.* **2020**, *32*, 1908194.

[26] Y. Guo, S. Zhang, M. Pu, Q. He, J. Jin, M. Xu, Y. Zhang, P. Gao, X. Luo, *Light Sci. Appl.* **2021**, *10*, 63.

[27] J. P. Balthasar Mueller, N. A. Rubin, R. C. Devlin, B. Groever, F. Capasso, *Phys. Rev. Lett.* **2017**, *118*, 113901.

[28] M. Liu, W. Zhu, P. Huo, L. Feng, M. Song, C. Zhang, L. Chen, H. J. Lezec, Y. Lu, A. Agrawal, T. Xu, *Light Sci. Appl.* **2021**, *10*, 107.

[29] H. F. Talbot, *London, Edinburgh Dublin Philos. Mag. J. Sci.* **1836**, *9*, 401.

[30] X. Qiu, F. Li, W. Zhang, Z. Zhu, L. Chen, *Optica* **2018**, *5*, 208.

[31] W. Meng, Y. Hua, K. Cheng, B. Li, T. Liu, Q. Chen, H. Luan, M. Gu, X. Fang, *Opto-Electronic. Sci.* **2022**, *1*, 220004.

[32] S. Liu, T. Cui, L. Zhang, Q. Xu, Q. Wang, X. Wan, J. Gu, W. Tang, Q. Qim, J. Han, W. Zhang, X. Zhou, Q. Cheng, *Adv. Sci.* **2016**, *3*, 1600156.

[33] L. Li, T. Cui, W. Ji, S. Liu, J. Ding, X. Wan, Y. Bo Li, M. Jiang, C. Qiu, S. Zhang, *Nat. Commun.* **2017**, *8*, 197.

[34] W. Fu, D. Zhao, Z. Li, S. Liu, C. Tian, K. Huang, *Light Sci. Appl.* **2022**, *11*, 62.

[35] X. Fang, H. Ren, M. Gu, *Nat. Photonics* **2019**, *14*, 108.

[36] H. Ren, X. Fang, J. Jang, J. Burger, J. Rho, S. A. Maier, *Nat. Nano-technol.* **2020**, *11*, 948.

[37] J. Sol, D. R. Smith, P. del Hougne, *Nat. Commun.* **2022**, *13*, 1713.

[38] M. Camacho, B. Edwards, N. Engheta, *Nat. Commun.* **2021**, *12*, 1466.

[39] F. Zhang, Y. Guo, M. Pu, X. Li, X. Ma, X. Luo, *Opto-Electron. Eng.* **2020**, *47*, 200366.

[40] N. Lassaline, R. Brechbühler, S. J. W. Vonk, K. Ridderbeek, M. Spieser, S. Bisig, B. le Feber, F. T. Rabouw, D. J. Norris, *Nature* **2020**, *582*, 506.

[41] N. A. Rubin, G. D'Aversa, P. Chevalier, Z. Shi, W. Chen, F. Capasso, *Science* **2019**, *365*, 43.

[42] X. Luo, M. Pu, Y. Guo, X. Li, F. Zhang, X. Ma, *Adv. Opt. Mater.* **2020**, *8*, 2001194.

[43] F. Yue, D. Wen, C. Zhang, B. D. Gerardot, W. Wang, S. Zhang, X. Chen, *Adv. Mater.* **2017**, *29*, 1603838.

[44] A. G. White, C. P. Smith, N. R. Heckenberg, H. Rubinsztein-Dunlop, R. McDuff, C. O. Weiss, C. Tamm, *J. Mod. Optic.* **1991**, *38*, 2531.

[45] D. Wen, F. Yue, G. Li, G. Zheng, K. Chan, S. Chen, M. Chen, K. Li, P. Wong, K. Cheah, E. Pun, S. Zhang, X. Chen, *Nat. Commun.* **2015**, *6*, 8241.

[46] E. D. Palik, *Handbook of Optical Constants of Solids II*, Academic Press, Boston, MA **1991**.